Preferential Sputtering induced Cr-Diffusion during Plasma Exposure of WCrY Smart Alloys

J. Schmitz[a,b,*], A. Mutzke[c], A. Litnovsky[a], F. Klein[a], X.Y. Tan[a,d], T. Wegener[a], P. Hansen[a], A. Eksaeva[a], M. Rasinski[a], A. Kreter[a], J. Gonzalez-Julian[a], J.W. Coenen[a], Ch. Linsmeier[a], M. Bram[a]

[a] *Forschungszentrum Jülich GmbH, Institut für Energie- und Klimaforschung, 52425 Jülich, Germany*
[b] *Department of Applied Physics, Ghent University, 9000 Ghent, Belgium*
[c] *Max-Planck-Institute for Plasmaphysics, Wendelsteinstrasse 1, 17491 Greifswald, Germany*
[d] *School of Materials Science and Engineering, Hefei University of Technology, Hefei 230009, China*

Abstract

WCrY Smart Alloys are developed as first wall material of future fusion devices such as DEMO. They aim at behaving like pure W during plasma operation due to depletion of the alloying elements Cr and Y. The Cr concentration gradients induced by preferential plasma sputtering cause Cr-diffusion. The exposure of WCrY and W samples to pure D plasma, with a plasma ion energy of 220 eV, is simulated using the dynamic version of SDTrimSP. Cr-diffusion is included into the model. Simulation results are compared with experimental results. At sample temperatures of more than 600 °C and sputtering by D plus residual oxygen in the plasma ion flux, the Cr-transport to the surface leads to enhanced erosion for WCrY samples. A diffusion coefficient for Cr in WCrY of the order of $1 \cdot 10^{-17}$ m^2/s is determined. The suitability of WCrY as first wall armour and the influence of further effects, considering especially Cr-diffusion, is discussed.

Keywords: smart alloys, plasma-wall-interaction, plasma ion irradiation, preferential sputtering, DEMO, modelling, diffusion, SDTrimSP

1. Introduction

Plasma-facing components (PFCs) of future fusion devices have to fulfill various requirements, which are described for example in [20]. Tungsten (W) is currently the preferred first wall material for the demonstration power plant DEMO. This material possesses various advantageous properties such as a very high melting point of more than 3300 °C and low erosion yields [3]. Yet, there are also some drawbacks regarding the usage of pure W: besides its inherent brittleness at room temperature, W oxidises rapidly at temperatures of above 700 °C, above 900 °C sublimation of the oxide becomes significant [19]. This makes pure W a potential safety hazard if a Loss-Of-Coolant-Accident (LOCA) with additional air ingress occurs. In that case the cooling system fails and the wall temperatures rise from 1000 °C to 1200 °C for a few days to several months, depending on the blanket design, due to nuclear decay heat [22]. W, having been activated by neutron irradiation during plasma operation, then forms radioactive WO_3. Sublimation of WO_3 leads to its mobilisation and thus the possible release of radioactive material out of the vacuum vessel. This has to be prevented to build safe fusion reactors.

Smart WCrY alloys aim at suppressing the oxidation of W during LOCA. These alloys contain, besides W, mainly chromium (Cr) and also small amounts of yttrium (Y). Their smartness consists in their ability to adapt to two kind of reactor scenarios: on the one hand, the lighter alloying elements Cr and Y are depleted towards the surface due to preferential sputtering during regular plasma operation. This leaves the plasma facing a pure W surface. In that way the material benefits from the low erosion yields of W. On the other hand, in case of LOCA with oxygen-containing atmosphere, the alloying elements diffuse towards the alloy's surface. A protective Cr_2O_3 scale forms and hence the formation of WO_3 is suppressed. The optimum composition for WCrY thin film systems was found to be W-11.4 wt%Cr-0.6 wt%Y, these are described in detail

*Corresponding author
Email address: jan.schmitz@fz-juelich.de (J. Schmitz)

in [36] and [21]. They demonstrated a significant oxidation suppression so that it was decided to produce bulk WCrY samples with the same composition. Bulk WCrY samples with the optimum composition achieved an oxidation suppression of more than three orders of magnitude in comparison to pure W samples of the same geometry. The oxidation rate was measured as gradient of mass change per area during oxidation in dry air at 1000 °C [29].

Given a convincing oxidation performance, the plasma performance of the WCrY smart alloys has to be evaluated. The alloys are developed for the first wall of DEMO. To choose relevant experimental conditions at first possible plasma conditions for the DEMO first wall are investigated: In [10] it is stated that a pulsed baseline DEMO reactor concept is prioritised with the possibility to be upgraded to a long-pulse or steady-state machine. The European DEMO design described in [38] assumes a peak heat flux of maximum 1 MW m^{-2} for the first wall. The first wall surface temperature during regular operation is restricted by the temperature limit of the considered structural material. The reduced activation ferritic martensitic steel EUROFER-97 [37] with a temperature limit of 550 °C [37] is one option considered for the European DEMO. The thermal conductivity of W is about $1 \cdot 10^2$ Wm^{-1}K^{-1} and tends to decrease under fusion-relevant radiation conditions [4]. [2] found a value of about $5 \cdot 10^1$ Wm^{-1}K^{-1} at temperatures between 500 °C and 700 °C for bulk WCrY samples with compositions similar to the one of the samples used for this work, which means a decrease in the thermal conductivity by a factor of two in comparison to pure W. Considering a 3 mm thick W or WCrY armour layer, first wall temperatures should not largely exceed 600 °C. Besides heat loads, particle loads of different origin strike the wall and can cause sputtering: plasma ions may be accelerated to energies exceeding the sputter thresholds, additional erosion is caused by charge exchange (CX) neutrals. In future fusion devices the erosion due to energetic neutrals is assumed to be of the same order of magnitude as for ions [27]. In some DEMO wall areas their contribution even dominates [34]. The thermal ions and other particles have a continuous energy distribution. Some particle energies lie above the sputter threshold, while the average stays below it. Temperatures in the DEMO Scrape-Off-Layer (SOL) are expected to be below 100 eV according to [37], whereas [14] expects more than 100 eV. The design question whether high heat flux limiters will be installed still remains open for DEMO [37]. When this limited configuration is used, e.g. during ramp-up or ramp-down of the plasma, the plasma gets closer to the wall and ion energies are elevated. Extrinsic impurity seeding can be used to reduce heat fluxes on PFCs. Concentrations of less than 1 % of argon (Ar) and xenon (Xe) or nitrogen (Ni) are foreseen for DEMO [16]. Moreover helium (He) produced by the deuterium-tritium (DT) reaction will always be present in the plasma. The heavy impurity species sputter W more effectively than the light hydrogen fuel ions.

In [30] it is stated that diffusion of Cr towards the surface is a determining factor for the erosion of WCrY at higher ion energies. Similarly, studies on W bombarded by energetic carbon (C) impurity ions presented in [31] underline the importance of thermally activated processes such as diffusion and segregation for the erosion of mixed materials. Therefore, in this publication we focus on modelling the plasma impact onto the alloy's surface composition including thermal diffusion. The effects of D ion irradiation, oxygen plasma content and Cr-diffusion are examined. Results obtained with the Monte-Carlo code SDTrimSP [24] are compared to experimental results.

2. Experimental

2.1. Plasma exposure

2.1.1. Description

The exposure to steady-state plasma took place in the linear plasma device PSI-2 [18]. In PSI-2 sputtering of a material is induced by bombardment with energetic ions. In contrast to the thermal particle energy distribution in DEMO, the ions during plasma exposure in PSI-2 are close to mono-energetic as determined by the applied bias voltage. Hence a DEMO-relevant ion energy has to be chosen for experiments. The PSI-2 plasma source was operated with pure D as working gas. However, a minute residual oxygen amount is present on Quadrupole Mass Spectrometry (QMS) data recorded in the PSI-2 vacuum vessel. The line radiation of the impurity oxygen was too weak to be detected with emission spectroscopy measurements, similar to the spectroscopy measurements described in [5] for an oxygen content of 0.2 % in PISCES-B. We therefore assume the oxygen impurity content to be of similar order as presented in [5]. In pure D plasma, no W sputtering is expected for ion energies of around 100 eV, as the sputter threshold for D on W is around 200 eV. For instance in [7] an experimental value of 178 eV as well as a fitted value of 201 eV are given. The W sputter threshold for residual oxygen in the plasma is considerably lower, in [7] the calculated threshold is 42 eV . To have W erosion caused by D sputtering and not only residual O, an ion

energy of 220 eV was chosen. The threshold for T on W is around 130 eV according to [7] and thus significantly lower in a D+T plasma than for pure D. As wall temperatures for the DEMO first wall should not be much higher than 600 °C (see chapter 1), the sample temperature during the PSI-2 experiments should also be in this range. The temperature of all sample surfaces is monitored during the exposure using an infra-red camera.

For the experiment two WCrY samples, called WCrY1 and WCrY2, and two W samples manufactured according to ITER specification [15], W1 and W2, were exposed simultaneously on the same target holder. WCrY samples had the optimum composition (see chapter 1) and were manufactured according to the procedure described in [30]. The four WCrY and W samples were all prepared in the same manner: after wire erosion cutting they were manually ground using silicon-carbide (SiC) paper. After grinding, the surface roughness R_a of the samples is about 30 nm. The samples were installed on a multi-target holder to expose them simultaneously to the plasma in PSI-2. To match the PSI-2 hollow plasma profile (see [18]) and ensure the same plasma conditions on all samples, they were placed in a circle at the same radial distance from the centre of the plasma column. The plasma flux hits the target at normal incidence and leads to heating of the samples to around 620 °C to 650 °C. The plasma is, besides the afore-mentioned residual oxygen, composed of singly ionised D+ ions. With an ion flux of $5.5 \cdot 10^{21}$ ions/(m^2s) a total accumulated fluence of about $1 \cdot 10^{26}$ ions/m^2 in about 5 h was reached. More experimental details are given in [30].

Two measurements are performed to evaluate the samples erosion: mass loss Δm and surface recession d_e. The mass loss Δm is obtained by weighing the samples before and after plasma exposure with a Sartorius MSA225P microbalance with a resolution of 10 µg. The surface recession d_e is obtained with the help of the Scanning Electron Microscope - Focussed Ion Beam (SEM-FIB) system (Carl Zeiss CrossBeam XB540): prior to plasma an orthogonal cut in the middle of a sample relative to the surface is created. For one sample an additional cut was done at the sample corner (WCrY2c). Equidistant markers are then generated on the orthogonal surface cut. The distance from the surface to the uppermost FIB marker is measured before and after plasma exposure. The distance from the receded surface to the uppermost FIB marker after plasma exposure is the surface recession d_e. In figure 1 the comparison of the distance between surface and uppermost FIB marker before and after plasma is shown and the surface recession d_e is indicated.

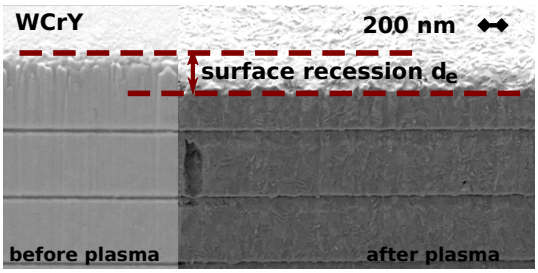

Figure 1: Comparison of the distance between surface and uppermost FIB marker before (left side) and after plasma (right side). The surface recession d_e is the difference between these two distances.

2.1.2. *Results*

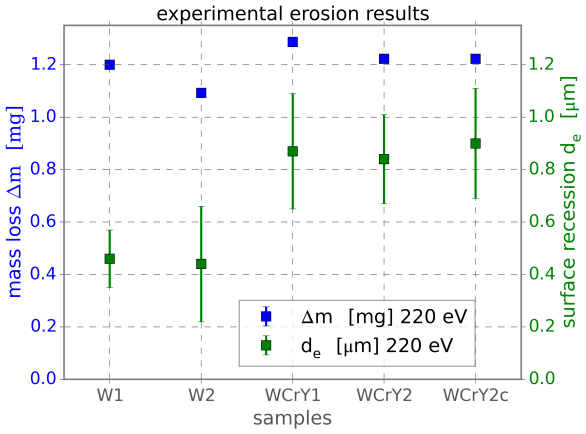

Figure 2: Comparison of mass loss Δm and surface recession d_e for pure W and WCrY samples. WCrY2c is a measurement taken at the corner of WCrY2. All other measurements were done in the respective sample centre.

Results for the samples' net erosion by weight loss Δm and the surface recession d_e are displayed in figure 2. Several values for d_e are measured and the average is taken, which explains the increased measurement uncertainty. All analysis processes are explained in detail in [30]. The mass loss Δm is very similar for all samples, around 1.1 mg for W and 1.2 mg for WCrY, whereas the surface recession d_e is nearly doubled for the WCrY with around 850 nm compared to the W samples with around 450 nm. This result indicates faster sputtering of WCrY. The alike values for d_e at the centre and corner of WCrY2 (WCrY2 and WCrY2c in figure 2, respectively) support the assumption that erosion is roughly homogeneous across the sample surface. We therefore define ρ_e, the density of the sputtered material, to be the

quotient of mass and volume loss:

$$\rho_e = \Delta m/\Delta V = \Delta m/(d_e \cdot A)$$

$$\approx 1200\ \mu g/(850\ nm \cdot 1\ cm^2) \approx 14.1\ g/cm^3$$

With an initial alloy composition of W-11.4 wt%Cr-0.6 wt%Y, which is equal to 67.9 at%W-31.1 at%Cr-1 at%Y[1], the initial theoretical density of the smart alloy is $\rho_{i,0} = 15.9\,g\,cm^{-3}$. Measurements according to the Archimedes principle confirmed an initial density of more than 98 %. Thus the minimum initial density ρ_i of the two smart alloy samples WCrY1 and WCrY2 is $15.9\,g\,cm^{-3} \cdot 0.98 = 15.6\,g\,cm^{-3}$. If the material is sputtered without significant mixing of material, the density of the eroded material ρ_e must approximately equal the initial material density ρ_i. Since the value of ρ_e is smaller than ρ_i, one can conclude that lighter elements were eroded proportionally more during plasma exposure.

2.2. Surface composition after vacuum heating

2.2.1. Experiment

The X-ray Photoelectron Spectroscopy (XPS)-device allows to heat samples to high temperatures under ultra-high-vacuum (UHV) conditions at a pressure of $1 \cdot 10^{-8}$ mbar to $1 \cdot 10^{-9}$ mbar. Moreover, the surface sensitive XPS analysis method can be used to monitor changes at the sample surface. The used XPS device is a PREVAC XPS setup equipped with an aluminium (Al) K_α X-ray source at an energy of 1.4867 keV. Whereas the sputtered area amounts to 5 mm × 5 mm, the analysis spot measures 1.6 mm × 5 mm. Assuming an exponential decay of the emission intensity within the sampled material, a sampling depth of $z = 3\lambda$ (the depth from which 95 % of the photoemission intensity is still detected for emission normal to the target surface) is estimated to be z = 5 nm in W, with λ from [17]. The XPS-setup was used to detect changes in the sample's surface composition, which are induced by heating under UHV conditions after preferential sputtering.

For this purpose one piece of sample WCrY1, ground according to the usual procedure used for plasma exposure, was used. First an SEM image (figure 3a) was taken, the sample was put into the XPS-device and the surface composition was measured (table 1a). Following this, the sample was heated to 900 K for 1 h, taken out and another SEM image was taken (figure 3b). Then the sample was put into the XPS device again and sputter-cleaned using 5 keV Ar ions before the surface composition was again analysed (table 1b). Subsequently, the sample was heated to 900 K for 3 h and another XPS analysis was carried out (table 1c). Eventually, the sample was taken out and another SEM image was taken (figure 3c). One should note that the SEM pictures are not taken at exactly the same position.

2.2.2. Results

The elongated scratches on the untreated sample surface in figure 3a stem from the grinding process during sample preparation. From table 1a it can be seen that there are residual impurities on the surface. The oxygen is mostly found as oxide bound to W and Cr. The 5 keV Ar-sputtering then leads to removing these impurities from the surface, the oxygen is decreased (table 1b). The measured molybden (Mo) stems from the sample holder inside the XPS device. As the sample piece was with dimensions of 5 mm × 4 mm only slightly larger than the measurement spot of size 1.6 mm × 5 mm, the analysis region can easily contain parts of the sample holder. Yet, we assume that this does not have an impact on the information we want to obtain, on the W and Cr presence in the sample surface. Further, fluorine (F) was found on the surface. This element has also been found by other analysis methods for samples produced and prepared around the same time. We assume that this fluorine stems from residual impurities on the equipment used for ultrasonic cleaning after the sample preparation procedure. The Ar-sputtering leads not only to a removal of an approximately 3 nm thick surface layer, but also to a characteristic surface morphology of small holes and elongated craters along the grain boundaries. The microstructure of WCrY features yttrium and oxide containing particles located at grain boundaries [30]. These are known to have the size of the order of tens of nm. The small black holes as well as the longer elongated craters are characteristic for smart alloys after being exposed to (plasma) ion irradiation and have been investigated in [30] and [29]. These features are caused by preferential sputtering of lighter elements and can still be seen on the SEM picture in figure 3c taken after heating of the sample for 3 h. It can be excluded that these features stem from heating the sample to 900 K since they are not observed in figure 3b after heating to this temperature for 1 h. For the XPS-analysis the Y content of the sample (1.0 at%) is close to the detection limit and not detectable after the Ar-sputtering (table 1b) due to preferential sputtering. The XPS-analysis results after heating for 3 h are shown in

[1] at%: atomic percent, elemental fraction of total atomic composition of alloy

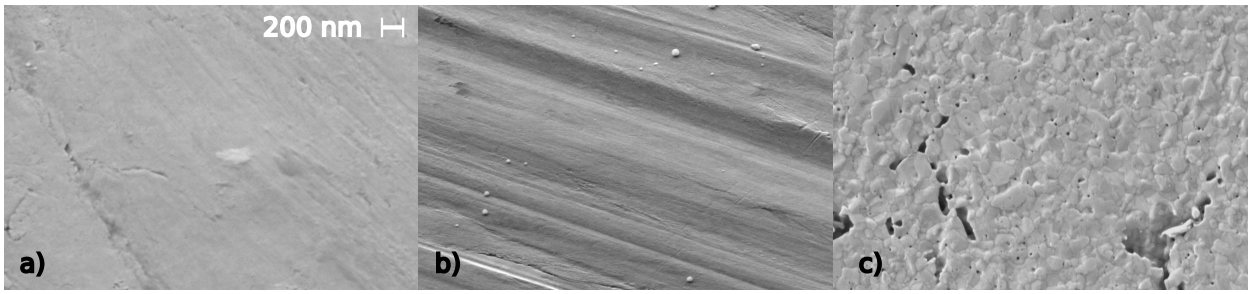

Figure 3: SEM images of the surface of the WCrY sample a) untreated, b) after heating to 900 K for 1 h and c) after Ar-sputtering and subsequent heating to 900 K for 3 h in UHV conditions.

	W [at%]	Cr [at%]	Y [at%]	other elements [at%]
a)	12.4 ± 0.2	3.4 ± 0.2	0.9 ± 0.1	34.0 ± 0.5 (O), 26.2 ± 0.8 (C), 0.4 ± 0.0 (Mo), 23.0± 0.5 (F)
b)	73.0 ± 1.1	14.9 ± 0.7	0.0	10.7 ± 1.2 (O), 1.4 ± 0.2 (Mo)
c)	63.8 ± 0.8	17.5 ± 0.6	0.0	18.1 ± 0.9 (O), 0.7 ± 0.2 (Mo)

Table 1: XPS-analysis of a piece of WCrY1 a) before Ar-sputtering, b) after Ar-sputtering and c) after Ar-sputtering and heating for 3 h to 627 °C

table 1c. The W surface coverage decreased and the oxygen as well as slightly the Cr surface coverage are increased after heating. Again, W and Cr are present in partly oxidised state. Hence, in UHV conditions and when the sample is heated after preferential sputtering Cr diffuses to the surface to form oxides so that less W is present.

3. SDTrimSP Modelling

3.1. Model description

The Monte-Carlo code SDTrimSP [24] makes use of the Binary-Collision-Approximation (BCA) to simulate ion irradiation of amorphous targets. The underlying physics is described in [6]. In the dynamic version a one-dimensional target made up of dynamically thickening or shrinking layers is employed. The ion projectiles successively shot into the target create recoils which in turn lead to reordering of atoms. Eventually, sputtering of atoms in the surface layer is caused if the energy transferred to these atoms is greater than the surface binding energy. Concentration gradients are induced in case of preferential sputtering for mixed materials. This means that the sputter yield, the number of atoms sputtered per incoming projectile, for one atomic species is higher than the yield of the other atomic species of the mixed material. With diffusion added to the model, the depleted element is transported towards the surface to counteract the build-up of these gradients. Owing to the usage of the dynamic version, we are able to look into the evolution of the alloy's near-surface composition. Since a one-dimensional target model is used, we do not reproduce the specific microstructure of the WCrY material but rather assume an amorphous target structure with a composition of 67.9 at%W-31.1 at%Cr-1 at%Y. The target is initially subdivided into equidistant 2.5 Å thick layers of the same composition. In a calculation step, a certain number of projectile ions, i.e. a certain fluence, is shot onto the target and their impact is calculated. After each such fluence step the target composition is updated according to the change in the number of the respective atomic species in each layer. If the composition is changed due to implantation or reordering of the recoils, this, in turn, causes a change in the atomic density. Implantation and recoils further result in an increase or ,in case of sputtering, decrease of the layer thickness. Summing over the changes in thickness of all layers leads to growth or shrinkage of the target. If erosion dominates the summation results in shrinkage, i.e. the surface recesses. For the calculations normal incidence of the bombarding ions is assumed. The samples' surface roughness

of about 30 nm cannot be reproduced with the one-dimensional model. This should not have a large impact on the erosion results for the case of normal incidence irradiation.

In SDTrimSP [24] thermal diffusion between adjacent target layers can be included into the model. For this purpose the temperature-dependent diffusion coefficients must be specified. Generally, diffusion is induced by concentration gradients of an element within a material. This is expressed by equation (1), which depicts the evolution of the element(i)-specific concentration c at layer x. The diffusion coefficient in equation (2) increases exponentially with temperature T. Diffusive transport across the surface boundary is set to zero. However, if atoms of the first layers get sputtered, the induced concentration gradient initiates diffusion from subsurface layers. The physical sputtering process within the model depends solely on the number of ions arriving at the target and not on the time as collisions are treated successively. In contrast, diffusion is a time-dependent process. Therefore, the ion flux, i.e. the number of ions arriving at the target per second, enforces a time dependence. The time for a fluence step results from equation (3), this time is then used to calculate a diffusion step. Calculated recoils result in changes of the concentrations c of the elements i within each layer x. Based on this concentration change, the overall layer-specific diffusion coefficient $\eta(x, i)$ (see equation (4)) is calculated. This is done by summing over the concentrations and diffusion coefficients of element i within material j for all elements j.

$$\frac{\partial c(i)}{\partial t} = -\frac{\partial(\eta(x,i) \cdot \frac{\partial c(x,i)}{\partial x})}{\partial x} \tag{1}$$

$$D(i,j) = D_0(i,j) \cdot \exp(-\frac{Q_a(i,j)}{k_B T}) \tag{2}$$

$$\Delta t = \frac{\Delta \text{fluence } [m^{-2}]}{\text{flux } [m^{-2}s^{-1}]} \tag{3}$$

$$\eta(x,i) = \sum^{j} c(x,j) \cdot D(i,j) \tag{4}$$

According to equation 2 two material-specific parameters have to be specified to assign a diffusion coefficient D(i, j) for element i in element j: the activation energy Q_a and the diffusion constant $D_0(i, j)$. Both are not known for the alloy WCrY. In order to vary only $D_0(i, j)$ for the simulations, we do not specify Q_a (see [23] for detailed explanation). Therefore, the simulations are only valid for the sample temperature present in the experiment. In that way a parameter scan for $D_0(i, j)$ can be performed. For the simple physical sputtering process, temperature is not taken into account within the BCA. The implementation of the algorithm solving the diffusion equation and further details are described in [35].

Lighter alloyed elements are preferentially sputtered, which leads to a continuous change of the surface stoichiometry during ion irradiation until a steady state is reached [32]. For this state the ratio of the sputter yields is stoichiometric [1]. This means for dynamical SDTrimSP runs partial sputter yields converge with increasing fluence (see figure 4b). In order to save computational time, simulations were carried out to a certain fluence and then extrapolated to the experimental fluence. Simulations shown here calculate 10 % of the experimental fluence, which is $1 \cdot 10^{26}$ ions/m^2 $\times$ $0.1 = 1 \cdot 10^{25}$ ions/m^2, assuming steady state has approximately been reached at this point. The last 10 values of this simulation are then used to linearly extrapolate the surface recession: the slope of a line intersecting these last 10 values is assumed to be constant until 100 % of the experimental fluence.

The mass loss is obtained from the simulation output by integration of the partial yield curves. Mass loss values were extrapolated using the partial sputter yields of W, Cr and Y at the last fluence step.

Experimental values are used for the adaptation of $D_0(i, j)$: the experimentally obtained surface recession d_e (see figure 2) is taken to be 450 nm for pure W and 850 nm for WCrY. Mass loss Δm reference values for W and WCrY are 1.1 mg and 1.2 mg, respectively. Both the measured mass loss and even more the surface recession are subject to measurement uncertainties (see figure 2), which is considered for determining the model parameters. Neither preferential sputtering nor diffusion have to be considered for the erosion yield of pure W samples.

3.2. Model results

In the following the effect of D ion irradiation, oxygen plasma content and Cr diffusion is presented according to their order of implementation in the model. Subsequently, effects of D retention, surface binding energies and possible other factors are examined.

3.2.1. Pure D irradiation

Sputter thresholds for pure W, Cr and Y calculated with SDTrimSP in static mode are shown in table 2. The thresholds for W and Cr are about 220 eV and 35 eV, respectively, and are approximately in agreement with the threshold values as presented in [33], 216 eV for W and

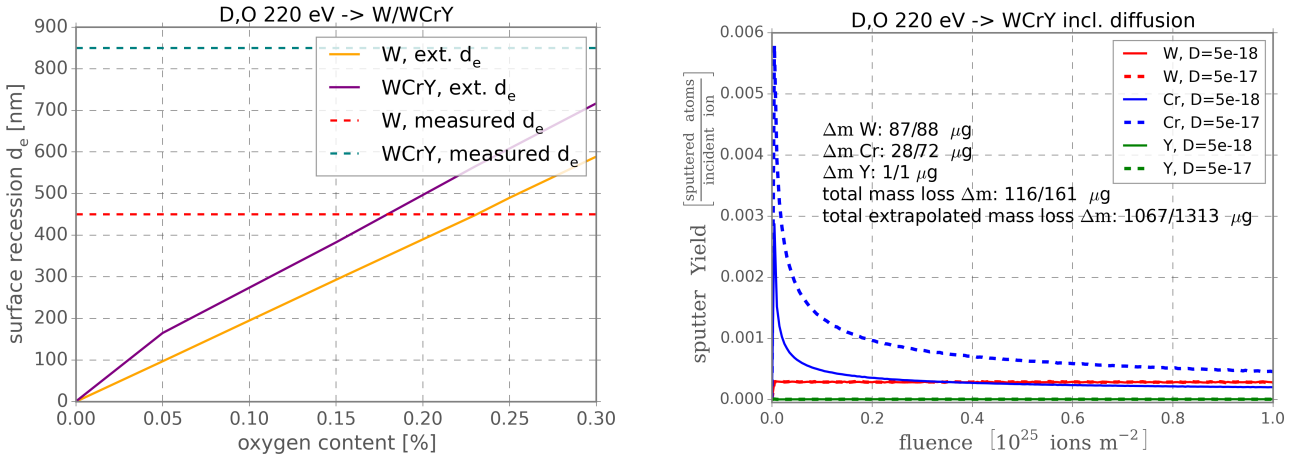

(a) (b)

Figure 4: SDTrimSP calculated surface recessions [nm] under D, O 220 eV ion bombardment: a) values for pure W and WCrY with mixed D, O ion irradiation with variation of the oxygen content O extrapolated (ext.) to the experimental fluence of $1 \cdot 10^{26}$ ions/m^2. Experimentally measured values for the surface recession d_e of W and WCrY are indicated by horizontal dotted lines. b) simulated partial sputter yields of W, Cr and Y for WCrY with the diffusion coefficient of Cr in WCrY, $D_{Cr,WCrY}$, set to $5 \cdot 10^{-18}$ m^2/s (continuous lines) and set to $5 \cdot 10^{-17}$ m^2/s (dashed lines). The mass loss per element is obtained via integration of the partial yield curves. Here the first value is the mass loss for $D_{Cr,WCrY}$ set to $5 \cdot 10^{-18}$ m^2/s and the second one the mass loss for $D_{Cr,WCrY}$ set to $5 \cdot 10^{-17}$ m^2/s.

target	bombarding ion species		
	D	O	Ar
W	220	45	35
Cr	35	20	20
Y	60	15	20

Table 2: Thresholds [eV] for pure elements W, Cr and Y sputtered by D, O and Ar as calculated with SDTrimSP at normal incidence using surface binding energies of 8.79 eV, 4.10 eV and 4.36 eV for W, Cr and Y, respectively.

34 eV for Cr. Oxygen sputter thresholds are considerably lower according to SDTrimSP: 45 eV for W and 20 eV for Cr. Especially at D ion energies close to or below the threshold, the effect of impurity oxygen becomes important [13]. Consequently, it can be expected that already small amounts of O in the target ion flux have a large impact on the material's erosion. Additionally, in the vicinity of Cr atoms, W atoms can get sputtered more easily due to an intermediate Cr-W collision [30]: according to the BCA the maximum elastic energy transfer between two colliding atoms 1 and 2 is

$$\gamma = 4m_1m_2/(m_1 + m_2)^2 \qquad (5)$$

$$\gamma_{D,W} \approx 0.04,\ \gamma_{D,Cr} \approx 0.14,\ \gamma_{Cr,W} \approx 0.69$$

$$\rightarrow\ \gamma_{D,Cr,W} \approx 0.10$$

With an intermediate Cr-W collision instead of the direct energy transfer from D to W the energy transfer factor γ is increased from 0.04 to 0.10. Thus in the vicinity of Cr atoms W sputtering is augmented. This effect is automatically included in the SDTrimSP model.
Surface recession results for W (yellow line) and WCrY (purple line) in pure D are shown in figure 4a, the first data point at x = 0 corresponds to an oxygen amount of 0.0 % in the plasma. For W the simulated surface recession amounts to only below 1 nm. This is far below the experimental value of 450 nm (red dotted line). Consequently, other factors influencing the sputter yield have to be considered.

3.2.2. Mixed D,O irradiation

The plasma oxygen content was varied in a next step. This value likely amounts to a few tenths of one percent of the plasma ion flux in PSI-2 (see chapter 2). In figure 4a surface recession versus varying oxygen content is displayed for both pure W and WCrY. Experimental surface recession of pure W (450 nm) is reproduced assuming a plasma composition of 99.73 % D and 0.23 % O, here the red dotted and yellow line intersect. Hence, this composition was used for further calculations. Whereas the experimentally obtained surface recession of pure W is matched by including oxygen, the WCrY surface recession of about 565 nm is far below the experimental value. There is no intersection point for the teal dotted

(WCrY, measured d_e) and the purple line (WCrY, ext. d_e) in figure 4a.

3.2.3. Mixed D,O irradiation including diffusion

To increase the sputtering of lighter alloying elements during the ion bombardment, these must be transported to the surface. The transport process was simulated by including thermal diffusion. For the variation of the diffusion coefficient of Cr in WCrY, $D_{Cr,WCrY}$, the oxygen content of the plasma is fixed to 0.23 %.

In order to calculate, besides the surface recession, also the mass loss from the simulations, the partial sputter yields are used. The evolution of the partial sputter yields of W, Cr and Y is displayed in figure 4b up to a fluence of $1 \cdot 10^{25}$ ions/m^2 for the diffusion coefficient $D_{Cr,WCrY}$ set to $5 \cdot 10^{-18}$ m^2/s (continuous lines) and set to $5 \cdot 10^{-17}$ m^2/s (dashed lines). All yield curves show an asymptotic trend towards increasing fluence, i.e. the sputter yields converge. The total mass loss is the sum of the partial mass losses for W, Cr and Y. Up to the calculated fluence the mass loss is obtained via integration of the yield curves, the yield obtained for the last fluence step is used for extrapolating the mass loss up to higher fluencies. On average, most of the mass loss is caused by W sputtering, whereas Cr sputtering is predominant at the beginning of the irradiation. The Cr partial sputtering yield is increased while W sputtering is at a low level because at first more Cr is present at the surface. In this state surface recession is accelerated compared to that of pure W. In the course of the irradiation Cr gets preferentially sputtered and less Cr atoms are present at the surface so that then more W is sputtered. Adding diffusion to the model leads to Cr transport towards the surface in case preferential sputtering creates Cr concentration gradients. For a higher diffusion coefficient the Cr transport towards the surface is stronger, provided a Cr concentration gradient exists. Stronger diffusion results in less pronounced Cr depletion at the alloy's surface, which means that the sputter yield of Cr is higher than that of W up to a higher fluence. Thus the overall mass loss is increased (1313 µg at $D_{Cr,WCrY} = 5 \cdot 10^{-17}$ m^2/s compared to 1067 µg at $D_{Cr,WCrY} = 5 \cdot 10^{-18}$ m^2/s) as the mass loss caused by Cr is increased (72 µg compared to 28 µg). Stronger diffusion can be caused either by a higher diffusion coefficient or by higher sample temperatures. However, the temperature was not varied in the simulations. Due to the small Y content in the sample, mass loss caused by Y sputtering does not play a significant role.

The diffusion coefficient was varied over several orders of magnitude. Surface recession values are calculated up to a fluence of $1 \cdot 10^{25}$ ions/m^2 and then extrapolated, results are shown in figure 5a. At 10 % of the experimental surface recession, i.e. 85 nm, the simulation results for 10 % of the experimental fluence match when choosing $D_{Cr,WCrY} = 5 \cdot 10^{-18}$ m^2/s. However, extrapolating the results of this simulation run to 100 % of the experimental fluence yields a surface recession value below the experimental one as can be seen in 5b: the extrapolated simulation yields a value of 723 nm (green line), which is below the experimental value of 850 nm (teal dotted line). With the aim of comparing extrapolated values to non-extrapolated ones, one calculation was performed for W (yellow line) and one for WCrY (purple line) up to a fluence of $1 \cdot 10^{26}$ ions/m^2. The diffusion coefficient $D_{Cr,WCrY}$ was set to $5 \cdot 10^{-18}$ m^2/s. Results are also shown in figure 5b: the non-extrapolated simulation yields a value of 660 nm (purple line), which is below the extrapolated value of 723 nm (green line). This is because the yield curves have not fully reached stationary conditions at the end of the simulated fluence. Since the surface recession is not yet strictly linear for WCrY, the model results deviate for later steps. Thus for more exactly determining the numerical value of the diffusion coefficient, simulations should be extended to 100 % of the experimental fluence. Yet, this would acquire very long computation times. Moreover, one has to take into account that the experimental surface and mass loss values are subject to measurement uncertainties which have an impact on the value of the diffusion coefficient as well. Consequently, for assigning a conclusive value to the diffusion coefficient, both the surface recession and the mass loss were considered.

The blue shaded bar in figure 5a indicates the range for the diffusion coefficient in which extrapolated simulation results either match the experimentally found surface recession d_e (left edge of the blue shaded bar) or the experimentally found mass loss Δm (right edge of the blue shaded bar). The diffusion coefficient has to be set to a value within the blue-shaded range in figure 5a, 2 to $3 \cdot 10^{-17}$ m^2/s.

3.3. Role of surface binding energy and retention

A further factor influencing the erosion yield of a material is the surface binding energy E_{SB}. This is the energy that a target surface atom needs to overcome to get sputtered. Generally, it is known that alloying leads to a decrease in surface binding energy. However, E_{SB} values for WCrY are not known. Commonly, for BCA models the heat of sublimation energy is used as an approximation for E_{SB}, as the actual E_{SB} values are unknown [39]. For W the default value in SDTrimSP tables is 8.79 eV. Lowering of E_{SB} to e.g. 6 eV for W in

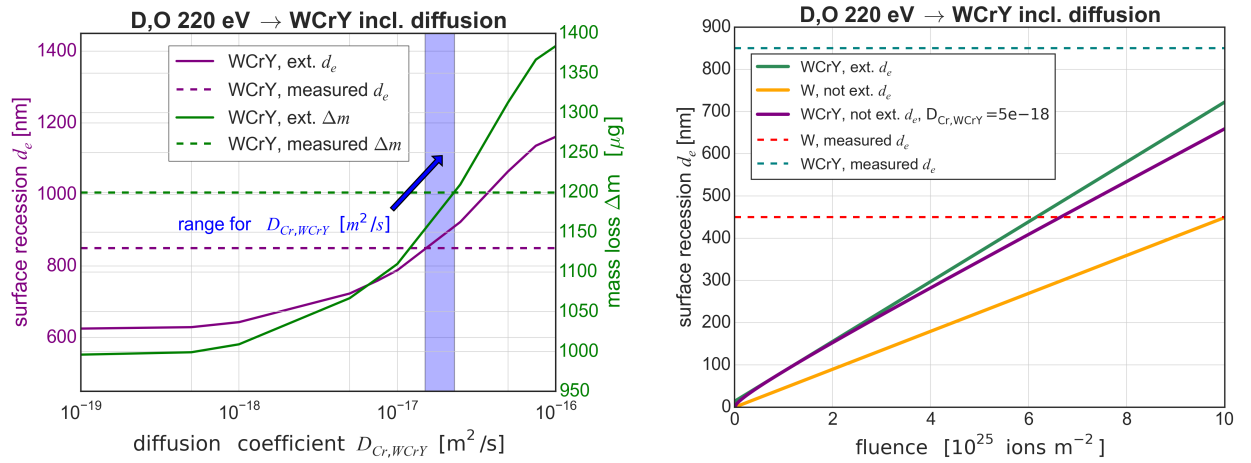

(a) (b)

Figure 5: SDTrimSP calculations under D, O (0.23 % O) 220 eV ion bombardment. a) shows the extrapolated (ext.) surface recession (sr) and mass loss (ml) for WCrY with varying diffusion coefficient. Experimentally measured values for the surface recession d_e and the mass loss Δm of WCrY are indicated by horizontal dotted lines. If the diffusion coefficient is set to a value within the blue shaded range, simulation and experimental results match. b) surface recession of pure W and WCrY (including diffusion with $D_{Cr,WCrY} = 5 \cdot 10^{-18}$ m^2/s) calculated for the experimental fluence of $1 \cdot 10^{26}$ ions/m^2 and not extrapolated (W and WCrY not ext.) and calculated for a fluence of $1 \cdot 10^{25}$ ions/m^2 and then extrapolated to the experimental fluence (WCrY ext.). Experimentally measured values for the surface recession d_e of W and WCrY are indicated by horizontal dotted lines.

WCrY at a plasma oxygen content of 0.23 % leads to an extrapolated surface recession of about 3 µm, at a mass loss of about 4.7 mg. This would mean a density of the eroded material of $\rho_e = 15.7\,g\,cm^{-3}$, which is about the initial density of the alloy (see chapter 2.1.2. Hence, a much lower surface binding energy of W in a mixed material may contribute to enhanced overall erosion. Yet, for explaining the reduced density of the eroded material, Cr-transport to the surface is needed.

For plasma-facing materials considering D retention is important. At the high sample temperatures of 620 °C to 650 °C during the experiment, D is easily released again and its content is hence very low when measured afterwards. [28] states that a higher intrinsic trap density in W-tantalum(Ta) alloys raises retention compared to pure W, while [40] finds no difference in the amount of retained H between W and W-Ta. D retention was found to be just slightly increased for WCrY compared to W when measured after the exposure [30]. Still, for a moment it may be present in the target during the exposure and hence influence the sputtering behaviour. When including D retention into the SDTrimSP model the target density is reduced with increasing the number of retained light D atoms. In that case less W is located at the target surface leading to a reduced W sputter yield. However, since there is no measurement of D retention during plasma exposure, the model is just used to qualitatively assess the influence of D retention on erosion yields.

In [11] and [26] a reduced energy threshold for oxidised W sputtered by light ions as compared to pure W is reported. This results from a decrease in the binding energy of tungsten oxide molecules. In SDTrimSP only binary atom collisions are considered and hence the effect of possible oxide formation is not taken into account.

4. Discussion

Comparison of experimental and simulation results for D ion irradiation on W and WCrY, including the effect of residual oxygen in the plasma, highlights the need for diffusion in the current model. By using the fact that, unlike a WCrY sample, the composition of a pure W sample does not change during plasma exposure, a value for the oxygen content of the plasma can be set (chapter 3.2.2). Here re-deposition and self-sputtering are not taken into account since results of the experimental erosion measurements represent the net erosion, not the gross erosion. SDTrimSP simulations do not include the effect of re-deposition. For estimating the effect of self-sputtering and re-deposition of W and Cr in PSI-2, ERO modelling was performed in other studies. ERO is a 3D Monte Carlo code used for simulating transport of sputtered particles. As described in

[8] there exists a version adapted to the PSI-2 geometry. Calculations employing this version and plasma parameters taken from measurements during the experiment were executed for pure W and Cr targets. The fraction of re-deposited material was calculated to be around 26 % in the case of W and 14 % for pure Cr. Hence an error is introduced as SDTrimSP calculates the gross erosion. Consequently, more W as well as WCrY may have been sputtered during the plasma exposure and the plasma oxygen content may be higher than 0.23 %.

After heating a WCrY sample for 3 h to 627 °C in the UHV conditions of the XPS device no W-oxides were found on the surface (2.2.2). Yet an increased Cr and O surface content was detected (see table 1 in 2.2.2). Thus, Cr must have diffused towards the surface to form oxides already at very low vacuum pressures. Potentially also during plasma exposure Cr-oxides may have been formed, adding to the effect of preferential sputtering of Cr. In SDTrimSP only binary atom collisions are considered, possible oxide formation is not taken into account.

In [35] simulations of coupled sputter-diffusion effects for a W-Fe system are presented. It was found out that when choosing a too narrow slab width in the target model, the algorithm used to solve the diffusion equations is prone to oscillatory behaviour. This is then reflected by oscillations in the surface concentrations. For the simulations presented in this work oscillatory behaviour was found neither for sputter yields nor for surface concentrations. This is why the initial layer width of 2.5 Å used in the target model is assumed to be appropriate to prevent the addition of synthetic effects to the Cr-diffusion process. The sharp decrease of the Cr partial sputter yield (figure 4b) can be ascribed to a W-enriched layer at the target surface. Similar experimental findings are presented for W-enrichment in CLF1 steel in [25] or EUROFER in [32].

Looking more closely on the numerical value for the diffusion coefficient, the following considerations were taken (see also 3.2.3): the partial sputter yields are approximately constant at 10 % of the experimental fluence and were thus used for extrapolation to 100 % of the experimental fluence to reduce computational time. Since the partial yields have not entirely converged, especially for Cr, values extrapolated to 100 % remain below the reference values for WCrY. The surface recession is approximately linear only when W partial sputtering dominates, after the lighter alloying elements have been depleted. Extending all simulations to 100 % experimental fluence would yield more exact surface recession and mass loss values at much higher computational costs. However, experimental measurement uncertainties and neglecting the influence of further factors as laid out in chapter 3.3, counteract the benefit of extending all simulations. Neglecting the influence of D retention, the Cr-diffusion in WCrY, $D_{Cr,WCrY}$, is likely greater than $5 \cdot 10^{-18}$ m^2/s and situated within the range of 2 to $3 \cdot 10^{-17}$ m^2/s.

5. Summary and outlook

WCrY and W samples were simultaneously exposed to pure D plasma at an ion energy of 220 eV in the linear plasma device PSI-2, net erosion and surface recession were measured. Already from calculating the density of the eroded material ρ_e it becomes evident that in case of WCrY lighter elements must have been transported towards the surface to be continuously sputtered and to lower the density of the eroded material (see 2.1.2). The XPS-treatment in chapter 2.2.2 gives experimental evidence for Cr diffusion to the surface at elevated sample temperatures after preferential sputtering. Diffusion of Cr in WCrY during ion irradiation causes increased surface recession and mass loss. One-dimensional SDTrimSP simulations showed that the effect of Cr-diffusion contributes to the erosion of WCrY samples during the plasma exposure with sample temperatures of 620 °C to 650 °C. Comparison of experimental and model results, taking into account also the plasma oxygen content, yields a diffusion coefficient of Cr in WCrY of the order of $D_{Cr,WCrY} = 1 \cdot 10^{-17}$ m^2/s. This value is valid for the temperature of the conducted plasma experiment.

The temperature of the first wall of future fusion devices such as DEMO could differ from the estimated temperatures of around 600 °C to 700 °C or fluctuate. Therefore, it is important to consider the influence of different temperature ranges on possible processes within the wall material. Temperatures of about 1000 °C will lead to both W- and Cr-oxidation. The latter subsequently leads to enhanced Cr erosion due to the elevated sputter yields of the oxide. According to [37] the damage of PFCs due to increased heat loads during disruptions as compared to regular operation is of great concern for DEMO. A higher temperature can lead to enhanced Cr-transport towards the surface, which results in increased erosion yields. Similarly, the effect of higher temperatures for the iron-tungsten (FeW) system is explained in [35]: high-Cr mobility suppresses build-up of gradients and therefore W enrichment. To investigate the temperature dependence of the W surface enrichment in WCrY, plasma exposure of samples at much higher and much lower temperatures than in the here described experiment in PSI-2 is envisaged. Better knowledge of the ac-

tivation energy Q_a for Cr-diffusion in the WCrY-system would help investigating the temperature dependence, yet this requires additional designated experiments and models.

For a material to be used as DEMO first wall material additional effects have to be considered: Effects of neutron irradiation induced transmutation of W and compositional changes on the material properties of W are complex and need to be considered for fusion operation [12]. For W alloys impacting neutrons can affect the different alloying elements in diverse ways. A good understanding of irradiation-induced segregation to grain boundaries of alloying and impurity elements is important also regarding mechanical properties of the material [9]. Especially Cr-segregation to the surface, contributing to the thermally activated diffusion, could, besides mechanical properties, affect the sputtering and oxidation performance of smart alloys.

The fraction of loss power radiated from the main chamber, the SOL and the divertor region has to be increased to solve the divertor power exhaust problem in DEMO. For this purpose impurity seeding is necessary [38]. Connected to the usage of different impurity species at different locations in the DEMO reactor, the gross and net erosion of PFCs at different locations has to be assessed. Here again for the smart alloys higher sputter yields of e.g. Ar (see table 2), Kr and Xe as compared to D and T may prevent the build-up of a sufficiently thick W-enriched layer. Enhanced Cr sputtering at temperatures of above 600 °C may lead to a significantly increased erosion of smart alloys as first wall components in comparison to a pure W first wall. Yet, impurity sputtering as well as CX neutrals and self-sputtering are a threat not only to WCrY but also to pure W wall components.

References

[1] R. Behrisch and W. Eckstein, eds. *Sputtering by Particle Bombardment: Experiments and Computer Calculations from Threshold to MeV Energies*. Vol. 110. Topics in Applied Physics. Berlin Heidelberg: Springer-Verlag GmbH, 2007. ISBN: 978-3-540-44502-9. DOI: 10.1007/978-3-540-44502-9.

[2] A. Calvo, K. Schlueter, E. Tejado, et al. "Self-passivating tungsten alloys of the system W-Cr-Y for high temperature applications". In: *International Journal of Refractory Metals and Hard Materials* 73 (2018), pp. 29–37. DOI: 10.1016/j.ijrmhm.2018.01.018.

[3] J. W. Coenen, S. Antusch, et al. "Materials for DEMO and reactor applications—boundary conditions and new concepts". In: *Physica Scripta* T167 (2016), p. 014002. DOI: 10.1088/0031-8949/2016/T167/014002.

[4] S. Cui, Russ P. Doerner, et al. "Thermal conductivity degradation and recovery in ion beam damaged tungsten at different temperature". In: *Journal of Nuclear Materials* 511 (2018), pp. 141–147. DOI: 10.1016/j.jnucmat.2018.09.002.

[5] R. P. Doerner, A. Grossman, et al. "Response of beryllium to deuterium plasma bombardment". In: *Journal of Nuclear Materials* 257.1 (1998), pp. 51–58. DOI: 10.1016/S0022-3115(98)00435-8.

[6] W. Eckstein. *Computer Simulation of Ion-Solid Interactions*. Vol. 10. Springer Series in Materials Science. Berlin and Heidelberg: Springer, 1991. ISBN: 978-3-642-73515-8. DOI: 10.1007/978-3-642-73513-4.

[7] W. Eckstein, Garcia-Rosales C., et al. "Sputtering Data: IPP-Report 9/82". In: (1993).

[8] A. Eksaeva, E. Marenkov, et al. "ERO modelling of tungsten erosion in the linear plasma device PSI-2". In: *Nuclear Materials and Energy* 12 (2017), pp. 253–260. DOI: 10.1016/j.nme.2017.03.014.

[9] R. G. Faulkner, S. Song, et al. "A model describing neutron irradiation-induced segregation to grain boundaries in dilute alloys". In: *Metallurgical and Materials Transactions A* 27.11 (1996), pp. 3381–3390. DOI: 10.1007/BF02595431.

[10] G. Federici, C. Bachmann, et al. "DEMO design activity in Europe: Progress and updates". In: *Fusion Engineering and Design* 136 (2018), pp. 729–741. DOI: 10.1016/j.fusengdes.2018.04.001.

[11] M.I Guseva, A.L Suvorov, et al. "Sputtering of beryllium, tungsten, tungsten oxide and mixed W–C layers by deuterium ions in the near-threshold energy range". In: *Journal of Nuclear Materials* 266-269 (1999), pp. 222–227. DOI: 10.1016/S0022-3115(98)00819-8.

[12] A. Hasegawa, M. Fukuda, et al. "Neutron irradiation effects on the microstructural development of tungsten and tungsten alloys". In: *Journal of Nuclear Materials* 471 (2016), pp. 175–183. DOI: 10.1016/j.jnucmat.2015.10.047.

[13] Y. Hirooka, M. Bourham, et al. "Evaluation of tungsten as a plasma-facing material for steady state magnetic fusion devices". In: *Journal of Nuclear Materials* 196-198 (1992), pp. 149–158. DOI: 10.1016/S0022-3115(06)80022-X.

[14] Y. Igitkhanov, B. Bazylev, et al. *Design Strategy for the PFC in DEMO Reactor (KIT Scientific Reports ; 7637)*. 2013. DOI: 10.5445/KSP/1000032116.

[15] ITER. "Material Specification for the Supply of Tungsten Plates for the ITER Divertor IDM No.ITERD2EDZJ4". In: *ITER Document* ().

[16] I. Ivanova-Stanik, M. Poradziński, et al. "Analysis of the optimum impurity mix for the EU DEMO scenario". In: *Fusion Engineering and Design* 136 (2018), pp. 1313–1316. DOI: 10.1016/j.fusengdes.2018.04.130.

[17] Y. Kamiura, K. Umezawa, et al. "Characterization of Polycrystalline Tungsten Surfaces Irradiated with Nitrogen Ions by X-ray Photoelectron Spectroscopy". In: *MATERIALS TRANSACTIONS* 57.9 (2016), pp. 1609–1614. DOI: 10.2320/matertrans.M2016107.

[18] A. Kreter, C. Brandt, et al. "Linear Plasma Device PSI-2 for Plasma-Material Interaction Studies". In: *Fusion Science and Technology* 68.1 (2015), pp. 8–14. DOI: 10.13182/FST14-906.

[19] E. Lassner and W. Schubert. *Tungsten: Properties, Chemistry, Technology of the Element, Alloys, and Chemical Compounds*. Boston, MA and s.l.: Springer US, 1999. ISBN: 978-1-4613-7225-7. DOI: 10.1007/978-1-4615-4907-9.

[20] Ch. Linsmeier, M. Rieth, et al. "Development of advanced high heat flux and plasma-facing materials". In: *Nuclear Fusion* 57.9 (2017), p. 092007. DOI: 10.1088/1741-4326/aa6f71.

[21] A. Litnovsky, T. Wegener, et al. "New oxidation-resistant tungsten alloys for use in the nuclear fusion reactors". In: *Physica Scripta* T170 (2017), p. 014012. DOI: 10.1088/1402-4896/aa81f5.

[22] D. Maisonnier, I. Cook, et al. "The European power plant conceptual study". In: *Fusion Engineering and Design* 75-79 (2005), pp. 1173–1179. DOI: 10.1016/j.fusengdes.2005.06.095.

[23] H. Mehrer, ed. *Diffusion in Solids: Fundamentals, Methods, Materials, Diffusion-Controlled Processes*. Vol. 155. Springer Series in Solid-State Sciences. Berlin Heidelberg: Springer-Verlag GmbH, 2007. ISBN: 978-3-540-71486-6. DOI: 10.1007/978-3-540-71488-0.

[24] Mutzke, A., Schneider, R., Eckstein, W. and Dohmen, R. *SDTrimSP Version 5.00 (IPP 12/8). Garching: Max-Planck-Institut für Plasmaphysik*. Tech. rep. 2011.

[25] L. Qiao, P. Wang, et al. "Erosion and deuterium retention of CLF-1 steel exposed to deuterium plasma". In: *Physica Scripta* T170 (2017), p. 014025. DOI: 10.1088/1402-4896/aa8c5c.

[26] J. Roth, J. Bohdansky, et al. *Data on low energy light ion sputtering: Report IPP 9/26*. Max-Planck-Inst. für Plasmaphysik, 1979.

[27] J. Roth, E. Tsitrone, et al. "Recent analysis of key plasma wall interactions issues for ITER". In: *Journal of Nuclear Materials* 390-391 (2009), pp. 1–9. DOI: 10.1016/j.jnucmat.2009.01.037.

[28] K. Schmid, V. Rieger, et al. "Comparison of hydrogen retention in W and W/Ta alloys". In: *Journal of Nuclear Materials* 426.1-3 (2012), pp. 247–253. DOI: 10.1016/j.jnucmat.2012.04.003.

[29] J. Schmitz, A. Litnovsky, et al. "Argon-seeded plasma exposure and oxidation performance of tungsten-chromium-yttrium smart alloys". In: *Tungsten* 455.1–3 (2019), p. 277. DOI: 10.1007/s42864-019-00016-7.

[30] J. Schmitz, A. Litnovsky, et al. "WCrY smart alloys as advanced plasma-facing materials – Exposure to steady-state pure deuterium plasmas in PSI-2". In: *Nuclear Materials and Energy* (2018). DOI: 10.1016/j.nme.2018.05.002.

[31] Tatyana Sizyuk and Ahmed Hassanein. "Effect of surface segregation and mobility on erosion of plasma-facing materials in magnetic fusion systems". In: *Journal of Nuclear Materials* 458 (2015), pp. 312–318. DOI: 10.1016/j.jnucmat.2014.12.105.

[32] K. Sugiyama, M. Balden, et al. "Erosion of EUROFER steel by mass-selected deuterium ion bombardment". In: *Nuclear Materials and Energy* 16 (2018), pp. 114–122. DOI: 10.1016/j.nme.2018.05.021.

[33] K. Sugiyama, K. Schmid, et al. "Sputtering of iron, chromium and tungsten by energetic deuterium ion bombardment". In: *Nuclear Materials and Energy* 8 (2016), pp. 1–7. DOI: 10.1016/j.nme.2016.05.016.

[34] M. Z. Tokar. "An assessment for the erosion rate of DEMO first wall". In: *Nuclear Fusion* 58.1 (2018), p. 016016. DOI: 10.1088/1741-4326/aa92dd.

[35] U. von Toussaint, A. Mutzke, et al. "Simulation of coupled sputter-diffusion effects". In: *Physica Scripta* T167 (2016), p. 014023. DOI: 10.1088/0031-8949/T167/1/014023.

[36] T. Wegener, F. Klein, et al. "Development of yttrium-containing self-passivating tungsten alloys for future fusion power plants". In: *Nuclear Materials and Energy* 9 (2016), pp. 394–398. DOI: 10.1016/j.nme.2016.07.011.

[37] R. Wenninger, R. Albanese, et al. "The DEMO wall load challenge". In: *Nuclear Fusion* 57.4 (2017), p. 046002. DOI: 10.1088/1741-4326/aa4fb4.

[38] R. Wenninger, R. Kembleton, et al. "The physics and technology basis entering European system code studies for DEMO". In: *Nuclear Fusion* 57.1 (2017), p. 016011. DOI: 10.1088/0029-5515/57/1/016011.

[39] X. Yang and A. Hassanein. "Atomic scale calculations of tungsten surface binding energy and beryllium-induced tungsten sputtering". In: *Applied Surface Science* 293 (2014), pp. 187–190. DOI: 10.1016/j.apsusc.2013.12.129.

[40] Y. Zayachuk, M.H.J. 't Hoen, et al. "Deuterium retention in tungsten and tungsten–tantalum alloys exposed to high-flux deuterium plasmas". In: *Nuclear Fusion* 52.10 (2012), p. 103021. DOI: 10.1088/0029-5515/52/10/103021.